Emergence of Sizeable Interfacial Dzyaloshinskii-Moriya Interaction at Cobalt/Fullerene Interface

Esita Pandey, Brindaban Ojha, and Subhankar Bedanta*

Laboratory for Nanomagnetism and Magnetic Materials (LNMM), School of Physical Sciences, National Institute of Science Education and Research (NISER), An OCC of Homi Bhabha National Institute (HBNI), Jatni 752050, Odisha, India

(Received 29 May 2022; revised 26 November 2022; accepted 12 January 2023; published 5 April 2023)

The interfacial Dzyaloshinskii-Moriya interaction (iDMI) originating from a heavy-metal/ferromagnet (FM) interface plays a crucial role in stabilizing chiral spin textures in magnetic multilayers. Recently, graphene based on the low-spin-orbit-coupling (SOC) element carbon (C) has shown a significant iDMI owing to the Rashba SOC when deposited on top of Co. A similar enhanced SOC has been reported earlier for other C allotropes, namely fullerene (C_{60}) and carbon nanotubes, and a sizeable DMI can be expected to emerge from them. In this context, we elucidate the magnetization-reversal mechanism, the domain-wall (DW) dynamics, and the strength of the iDMI in a Pd(4.0 nm)/Co(0.5 nm)/C_{60}($t_{C_{60}}$)/Pd(2.0 nm) system with varying $t_{C_{60}}$. The field-induced DW velocity measured in the creep region shows a DW velocity 2 orders of magnitude higher for a sample with 1.6 nm of C_{60}, due to a lower depinning field and spin-dependent hybridization at the Co/C_{60} interface. Further, DMI measurements performed by use of the asymmetric DW expansion method exhibit a systematic increase in the iDMI from -0.07 to -0.46 mJ/m^2 with an increase in $t_{C_{60}}$. Such an enhanced iDMI turns an achiral Bloch wall into a chiral Néel wall. The emergence of a finite DMI ($D_{Co/C_{60}} \sim -0.11$ mJ/m^2) from the Co/C_{60} interface is particularly encouraging for the use of C-based materials in chiral-DW-based device applications.

DOI: 10.1103/PhysRevApplied.19.044013

I. INTRODUCTION

The new generation of spin logic devices are aimed at storing and processing information in magnetic nanostructures, i.e., domain walls (DWs) and/or skyrmions, to increase storage density and reduce power consumption [1,2]. Further, the storing and processing of information requires spin transport over a long distance at a faster speed with negligible scattering [3–5]. Hence a material combination that allows one to acquire both a chiral spin texture and a long spin-transport channel in a single heterostructure is preferred [6–9].

C-based materials, e.g., fullerene (C_{60}), graphene, and carbon nanotubes (CNTs), are important in spintronic applications as they provide a long spin diffusion length, a large spin relaxation time, and less hyperfine interaction than in other materials [5,10,11]. All of these carbon allotropes (e.g., C_{60}, graphite, and CNTs) can be formed from a single structural unit known as graphene. The low atomic number of C and the absence of hydrogen (H) atoms in these allotropes help one to transport spin information over a long distance without scattering [4]. In addition, a fullerene molecular layer also helps to reduce the impedance-mismatch issue by forming a hybridized interface when placed next to a ferromagnet (FM). In a FM/C_{60} heterostructure, broadening and shifting of the molecular density of states occur primarily due to spin-dependent orbital hybridization [12]. This results in an effective hybridized interface known as an "organic spinterface." Such a spinterface acquires a net spin polarization and modulates the magnetic properties (e.g., magnetic anisotropy, magnetoresistance, saturation magnetization, and domain structure) of both the FM and the organic molecular layer [12–17]. However, it is noteworthy that fullerene can also induce a perpendicular magnetic anisotropy (PMA) in a FM (Co) film by reducing the in-plane anisotropy contribution of the d_{z^2} orbital [18,19]. A similar enhancement of the PMA has also been observed in a graphene/FM system, where the magnetic anisotropy (MA) contribution of the d_{z^2} and d_{yz} orbitals was found to be altered [20,21]. Although the origin of the PMA in a FM/heavy-metal (HM) system with a high spin-orbit coupling (SOC) is well established, the emergence of the same in a FM/C-based system appears to be a result of a change in the orbital anisotropy and an enhanced SOC in the allotropes. Even though these materials are composed of light elements, an enhanced SOC has been reported for C-based materials (viz. fullerene, CNTs, and graphene), owing to their curved

*sbedanta@niser.ac.in

structure and Rashba-type interactions [22–24]. The curvature of the buckyball structure helps in electron hopping between the adjacent π and σ bonds of the C atoms, which generates an additional SOC along with the weak intrinsic SOC [23–26]. Therefore, C-based materials may also aid in the creation of a significant Dzyaloshinskii-Moriya interaction (DMI) when deposited on top of a FM [7,8,27].

It is worth mentioning that the DM interaction is a key parameter in controlling and optimizing the efficiency of chiral-domain-wall-based devices and hence has been studied thoroughly in the last few years [28–31]. A DMI that originates at the interface of a FM/HM heterostructure due to the lack of inversion symmetry is known as an interfacial DMI (iDMI). In the case of a symmetric $HM_1/FM/HM_1$ system, the absence of an iDMI leads to the formation of an achiral Bloch wall (BW), whereas an asymmetric system gives rise to a sizeable iDMI, which may transform a BW into a chiral Néel wall (NW) and increase the DW velocity significantly [30–33]. In the case of FM thin-film and multilayer systems, such an iDMI helps in the creation and stabilization of skyrmions [34]. Thus, tailoring the strength of the iDMI and the velocity of the DWs is indispensable for realizing high-density, faster chiral DW-based devices. A few recent studies have revealed that the Rashba-interaction-mediated high SOC of graphene can generate a significant Rashba DMI at a graphene/Co interface, which induces a chiral Néel wall structure [7,8,27]. Thus, C-based materials appear to be a promising alternative to HMs for inducing an iDMI, generating a chiral wall structure, and reducing the scattering of information while it is being transferred through a long spin-transport channel. These studies motivate us further to explore the efficiency of other C-based materials (e.g., fullerene and CNTs) for tuning the DMI, chiral wall structure, and DW dynamics when deposited next to a HM/FM system. In the work presented here, Pd/Co is selected as a standard HM/FM system, due to a recent demonstration of the emergence of a significant spin-orbit torque from nanowires in Co/Pd multilayers [35].

A series of $Pd/Co/C_{60}(t_{C_{60}})/Pd$ samples are prepared by varying the thickness of the fullerene layer to unravel how the strength of the DMI, the chirality of the DW, and their dynamics can be tailored by considering a fullerene/Co spinterface. A significant enhancement in the magnetization relaxation mechanism is observed, which is attributed to a decrease in the depinning field and an increase in the DW velocity upon C_{60} insertion. Notably, the DW structure also changes from an achiral Bloch wall ($t_{C_{60}} = 0$ nm) to a left-handed chiral NW ($t_{C_{60}} = 1.6$ nm) owing to an enhancement in the iDMI from -0.07 mJ/m^2 ($t_{C_{60}} = 0$ nm) to -0.46 mJ/m^2 ($t_{C_{60}} = 1.6$ nm) in the asymmetric $Pd/Co/C_{60}$ samples. As the DMI helps to improve the degeneracy of the chiral wall here, we extract the strength of the iDMI originating from the Co/C_{60} interface and find a nonzero iDMI contribution, possibly due to the curvature-enhanced SOC of fullerene.

II. EXPERIMENTAL DETAILS

A series of samples are prepared by varying $t_{C_{60}}$, where the structure is as follows: Si(100)/Ta(10 nm)/Pd(4 nm)/Co(0.5 nm)/$C_{60}(t_{C_{60}})$/Pd(2 nm)/Ta(3 nm). The samples are named S1, S2, and S3, with $t_{C_{60}} = 0$, 0.8, and 1.6 nm, respectively. All of the metallic layers (Ta, Pd, and Co) are deposited by dc magnetron sputtering, whereas the organic layer (C_{60}) is deposited by a thermal evaporation technique at a base pressure of 6×10^{-8} mbar in a high-vacuum multideposition chamber. Further details regarding sample preparation are mentioned in the Supplemental Material [36]. X-ray reflectivity (XRR) measurements are performed to quantify the structural parameters (e.g., thickness, roughness, and density) of the multilayer samples using an x-ray diffractometer, and details are given in the Supplemental Material [36]. The magnetization relaxation, field-induced DW dynamics, and iDMI strength (via the asymmetric DW expansion method) are measured using magneto-optic Kerr effect (MOKE) based microscopy (called as Kerr microscopy) [37]. The magnetic anisotropy is quantified from M-H loops measured by a superconducting quantum interference device (SQUID) at room temperature. A detailed measurement protocol can be found in the Supplemental Material [36].

III. RESULTS AND DISCUSSION

A. Magnetization reversal

Polar MOKE hysteresis loops for samples S1–S3 are shown in Fig. 1(a), where the coercivity ($\mu_0 H_c$) decreases systematically with increasing C_{60} coverage. Such a decrease in $\mu_0 H_c$ reflects a decrease in the effective PMA in the samples caused by substituting the top Pd layer with a C_{60} layer. Here, $\mu_0 H_c$ decreases systematically from 15.98 mT (in S1) to 3.12 mT (in S3), indicating a magnetic softening along with a sharp magnetization reversal upon C_{60} insertion. In contrast to the 3d-4d hybridization that should arise at the top Co/Pd interface [38–40], the deposition of an organic layer (C_{60}) on top of Co results in an interfacial hybridization between C p and Co 3d orbitals [18,19]. Such hybridization leads to the formation of a spinterface at the Co/C_{60} interface and modifies the magnetic anisotropy, as well as the coercive field of the samples [19,41–43]. Because of the interfacial nature of the hybridization, a reduction in coercivity is observed until the formation of a 1.6-nm-thick C_{60} layer in S3. A minor change in magnetic characteristics might be anticipated upon the formation of 2 monolayers of fullerene, followed by no discernible change with further increase in $t_{C_{60}}$ [12].

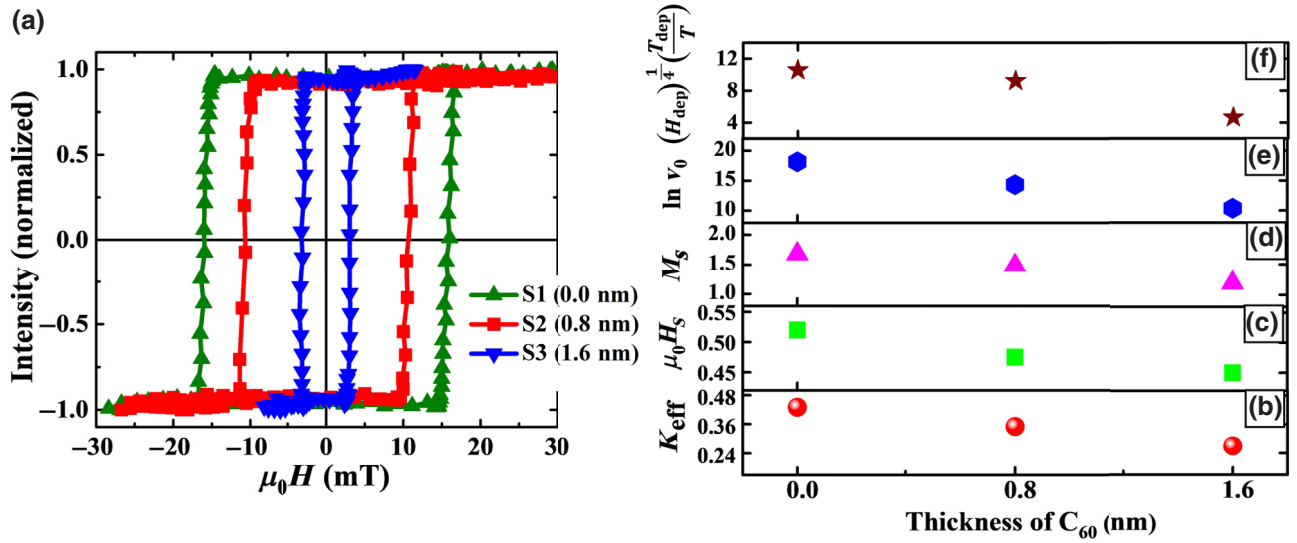

FIG. 1. Magnetic properties of Pd(4 nm)/Co(0.5 nm)/C_{60}($t_{C_{60}}$)/Pd(2 nm) samples: (a) hysteresis loops measured by polar MOKE microscopy; (b)–(d) values of K_{eff} (in MJ/m^3), $\mu_0 H_s$ (in T), and M_s (in MA/m) measured by a SQUID magnetometer; (e),(f) values of $\ln(v_0)$ and $(H_{\text{dep}})^{1/4}(T_{\text{dep}}/T)$ extracted from the DW velocity measurements using MOKE microscopy.

B. Magnetic anisotropy

M-H loops are measured along both the in-plane (IP) and out-of-plane (OP) directions of the samples, as shown in the Supplemental Material [36], to quantify the effective magnetic anisotropy (K_{eff}) using the formula $K_{\text{eff}} = \frac{1}{2}\mu_0 H_s M_s$, where $\mu_0 H_s$ is the IP saturation field and M_s is the saturation magnetization [44]. Values of K_{eff}, $\mu_0 H_s$, and M_s for all the samples are listed in Table I and plotted in Fig. 1(b)–1(d). Because of the high electron affinity of C (2.6 eV), spin-polarized charge transfer may occur from Co to C_{60}, giving rise to the observed reduction in saturation magnetization in the Pd/Co/C_{60} samples [11,18,19,45]. The role of the Co/C_{60} interface in magnetic softening can be well understood by analyzing the nature of the orbital hybridization that occurs at the Co/C_{60} interface. In a fullerene molecule, each C atom forms three σ bonds (between sp^2 orbitals) and one π bond (between p_z orbitals) with the neighboring C atoms [46]. As the p_z orbitals of fullerene spread more into the exterior of the molecule than into the interior, they make a strong bond with the 3*d* orbitals of a ferromagnetic metal when placed next to it. Hybridization between the p_z-d_{xy,x^2-y^2} and/or p_z-$d_{yz,zx}$ orbitals leads to a reduction in the PMA at the interface in the Co/C_{60} system. Notably, for a Pd/Co/Pd system, a density-functional-theory (DFT) calculation indicates that both the $3d_{xy,x^2-y^2}$ and the $3d_{yz,zx}$ orbitals of Co give rise to a PMA at the interface [39]. In our case, we expect that a similar hybridization occurs between the p_z-d_{xy,x^2-y^2} and p_z-$d_{yz,zx}$ orbitals, leading to a decrease in the effective PMA of the system. Future DFT calculations may shed light on the exact nature of hybridization related to the occurrence of magnetic softening in such systems. Apart from the spinterface, the strength of the magnetic anisotropy for a Co/C_{60} system also depends on the choice of buffer layer (e.g., Pd, Pt, or Au) and the adsorption geometry (either hexagonal or pentagonal rings of C) of the C_{60} molecules upon the FM layer. The decrease in the MA landscape is consistent with the decrement in coercivity as observed from the hysteresis loops. It has been reported earlier that the spinterface thickness in a FM/organic molecular system can extend up to 2–3 nm, and hence, for higher thicknesses of C_{60}, a minor change in anisotropy is possible [16].

C. Relaxation dynamics

In order to further understand the effect of spinterface formation on the magnetization-reversal phenomena here, we perform magnetization relaxation measurements on all of the samples. Such relaxation measurements provide a clear understanding of the impact of thermal activation energy on the completion of the reversal process at a constant applied magnetic field (or Zeeman energy). A detailed measurement protocol can be found in the Supplemental Material [36]. Here, the experimental data are fitted by a compressed exponential function, written as [47–50],

$$I(t) = I_1 + I_2\left(1 - \exp\left(-\left(\frac{t}{\tau}\right)^{\beta}\right)\right), \qquad (1)$$

where $I(t)$ is the Kerr intensity measured at time t, $I_1 + I_2$ is the normalized Kerr intensity, β is an exponent varying from 1 (nucleation-dominated relaxation) to 3 (DW-motion-dominated relaxation), and τ is the relaxation time constant. A faster relaxation process is observed in samples S2 ($\tau = 12.70 \pm 0.13$ s) and S3 ($\tau = 10.50 \pm 0.20$ s)

TABLE I. Parameters of the Pd/Co/C_{60}/Pd multilayer samples (S1–S3).

Sample name	$\mu_0 H_c$ (mT)	τ (s)	$\mu_0 H_s$ (mT)	M_s (MA/m)	K_{eff} (MJ/m^3)	$\delta = \sqrt{A/K_{\text{eff}}}$ (nm), $A = 14$ pJ/m	$\mu_0 H_{\text{DMI}}$ (mT)	$D_{\text{eff}} = \mu_0 H_{\text{DMI}} M_s \delta$ (mJ/m^2)
S1	15.98	19.70 ± 0.21	520	1.66	0.43 ± 0.010	5.69 ± 0.06	8.09	-0.077 ± 0.015
S2	10.70	12.70 ± 0.13	475	1.45	0.34 ± 0.007	6.42 ± 0.07	18.70	-0.174 ± 0.018
S3	3.12	10.50 ± 0.20	450	1.20	0.27 ± 0.006	7.21 ± 0.08	53.40	-0.462 ± 0.013

in comparison with sample S1 ($\tau = 19.70 \pm 0.21$ s). For sample S2, as the fullerene layer is very thin, it forms an intermixed Co-C_{60}-Pd layer rather than a continuous layer of C_{60}, leading to a decrease in the domain size and an increase in the domain nucleation density. This increased domain nucleation density helps to achieve a faster relaxation in sample S2 than in sample S1 (see the Supplemental Material [36]). However, for sample S3, as the thickness of the fullerene layer is much higher than the roughness, the fullerene forms a continuous layer, unlike the case for sample S2. The formation of a continuous fullerene layer and hence a spinterface at the Co/C_{60} interface leads to a significant reduction in the PMA, which reduces the DW formation energy ($\sigma = 2\pi\sqrt{AK_{\text{eff}}}$) in the sample. Further, a reduced DW formation energy induces a higher DW velocity and initiates a faster relaxation mechanism in sample S3 in comparison with S1. The Supplemental Material contains a thorough explanation of the faster relaxation mechanism observed in both sample S2 and sample S3 [36].

D. Domain-wall dynamics

To unravel the role of the fullerene molecular layer in the DW dynamics, we perform pulsed magnetic-field-driven DW velocity measurements. As the multilayer samples studied in the work presented here are ultrathin in nature, the motion of the DWs can be considered similar to the motion of a one-dimensional elastic interface in a two-dimensional disordered medium. Such a DW dynamics is generally divided into three regimes, namely creep, depinning, and flow [51]. At $T = 0$ K, the DW moves only after a critical threshold field H_{dep} is reached ($H_{\text{OP}} > H_{\text{dep}}$). However, at $T \neq 0$ K, a DW can move even in a field lower than H_{dep}. Here, thermal activation energy helps the DW to overcome the pinning barrier, resulting in a very slow motion known as "creep." In the work presented here, we study the effect of spinterface formation (at the Co/C_{60} interface) in this creep region of DW motion, which obeys an Arrhenius law, written as [51,52],

$$v_{\text{DW}} = v_0 \exp\left[-\frac{U_c}{k_B T}\left(\frac{H_{\text{OP}}}{H_{\text{dep}}}\right)^{-(1/4)}\right], \qquad (2)$$

where v_0 is the scaling parameter of the velocity, $U_c = k_B T_{\text{dep}}$ is the height of the pinning potential, $k_B T$ is the thermal activation energy, and H_{dep} is the depinning threshold field. The logarithm of Eq. (2) gives a linear relation between $\ln(v_{\text{DW}})$ and $(H_{\text{OP}})^{-(1/4)}$, which can be written as

$$\ln(v_{\text{DW}}) = \ln(v_0) - \frac{T_{\text{dep}}}{T}\left(\frac{H_{\text{OP}}}{H_{\text{dep}}}\right)^{-(1/4)}. \qquad (3)$$

Figure 2 presents plots of the DW velocity (v_{DW}) versus the applied field ($\mu_0 H_{\text{OP}}$) and of $\ln(v_{\text{DW}})$ versus $(\mu_0 H_{\text{OP}})^{-(1/4)}$ for varying $t_{C_{60}}$. The experimental data are fitted well by Eqs. (2) and (3), and this confirms that the DW motion lies in the creep region for all of the samples. It is evident from Fig. 2 that at a constant magnetic field (say, approximately 10 mT), the DW velocity in sample S3 is considerably higher than in the reference sample, S1. A few possible explanations for this velocity increment are as follows: lowering of the depinning field (H_{dep}), a reduction in the effective PMA (K_{eff}), a modified DW structure (from Bloch to Néel), and an enhanced DM interaction in the Pd/Co/C_{60} samples. The values of $\ln(v_0)$ and $(H_{\text{dep}})^{1/4}(T_{\text{dep}}/T)$ are extracted by fitting the experimental data in Fig. 2 by Eqs. (2) and (3). The extracted data are plotted in Figs. 1(e) and 1(f). The depinning field (H_{dep}) is strongly related to the defects present in the system and represents a local variation in the anisotropy landscape. Modification of the local anisotropy is also viable for systems with a hybridized interface (e.g., Co/C_{60}). In our case, the ratio of $(H_{\text{dep}})^{1/4}(T_{\text{dep}}/T)$ is reduced nominally from 10.56 (for sample S1) to 9.22 (for sample S2), leading to comparable DW velocities in samples S1 and S2. Notably, for sample S2, the fullerene layer is very thin (approximately 0.80 nm) and its thickness is comparable to its roughness; hence, a continuous layer is quite unlikely to form. Here, the C_{60} acts as a dusting layer, and at some places the top Pd layer may be in direct contact with the Co layer, leading to the formation of an intermixed Co-C_{60}-Pd layer (see the XRR fit in the Supplemental Material [36]). This affects the growth quality of the film, increases the interfacial roughness, and modifies the anisotropy landscape locally. Therefore, compared with sample S1, a higher domain nucleation density, smaller domain size, and comparable DW velocity are found for sample S2. However, for sample S3, as the thickness of the fullerene layer (approximately 1.60 nm) is greater than its roughness (approximately 0.70 nm), the fullerene layer became continuous with reduced pinning sites. Therefore,

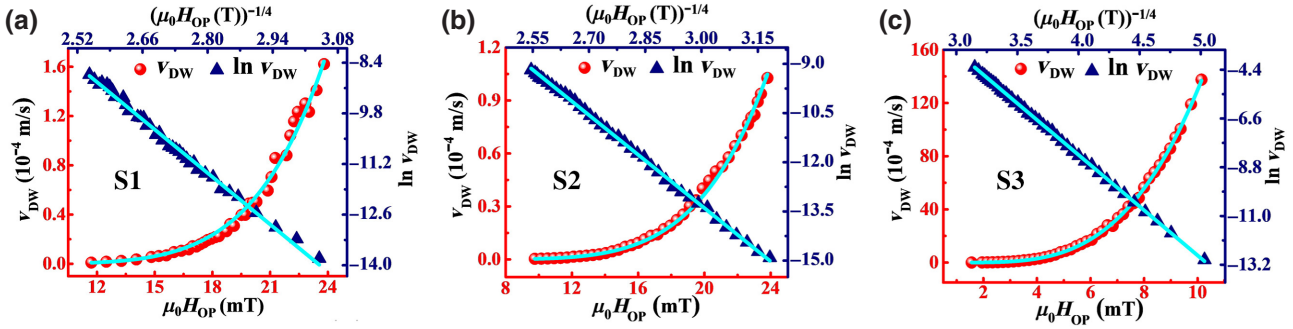

FIG. 2. Plots of DW velocity (v_{DW}) versus $\mu_0 H_{OP}$ and $\ln(v_{DW})$ versus $\mu_0 H_{OP}^{-(1/4)}$ for samples S1 (a), S2 (b), and S3 (c). Here, $\mu_0 H_{OP}$ represents the pulsed magnetic field applied along the OP direction. The solid lines represent the best fits of the curves to the creep law.

the ratio of $(H_{dep})^{1/4}(T_{dep}/T)$ is found to decrease significantly from 10.56 (for sample S1) to 4.65 (for sample S3), which supports the observed enhancement of the DW velocity. Thus, sample S3 does not form small-size bubble domains with a high domain nucleation density as sample S2 does. Further, a considerable decrease in the PMA (approximately 37%) aids in lowering the DW formation energy (σ) in sample S3, which in turn helps to achieve a higher DW velocity. In addition, the DMI strength is also found to increase from -0.077 (for sample S1) to -0.46 mJ/m^2 (for sample S3), which turns the Bloch wall into a Néel wall and supports the observed increase in DW velocity in sample S3 (details are given in Sec. III E). Since the orbital hybridization, charge transfer, and curvature-enhanced SOC at the Co/C_{60} interface are responsible for a considerable reduction in the PMA and improvement in the iDMI strength in sample S3, the insertion of a continuous fullerene layer plays an important role in tailoring the DW velocity. It is worth mentioning that for sample S2, the DW motion may be constrained by local variation in the anisotropy landscape, which hinders any increase in the DW velocity despite a minor decrease in the PMA and a rise in the DMI strength.

E. Dzyaloshinskii-Moriya interaction

According to the Fert and Levy model, the DM interaction originates at the interface of a HM/FM system as a consequence of broken inversion symmetry and the high SOC of the HM. In our case, as the reference sample S1 is symmetric in nature (Pd/Co/Pd), a very minimal DMI can be expected to emerge. However, the insertion of an organic C_{60} layer breaks the inversion symmetry (by creating a Pd/Co/C_{60} structure) and may introduce a nonzero DMI arising from the Co/C_{60} interface. The SOC in C-based materials is considered to be weak due to the low atomic number of C ($Z = 6$). However, the SOC in fullerene is composed of two parts: (i) an intrinsic SOC (Δ_{int}), whose strength is small due to

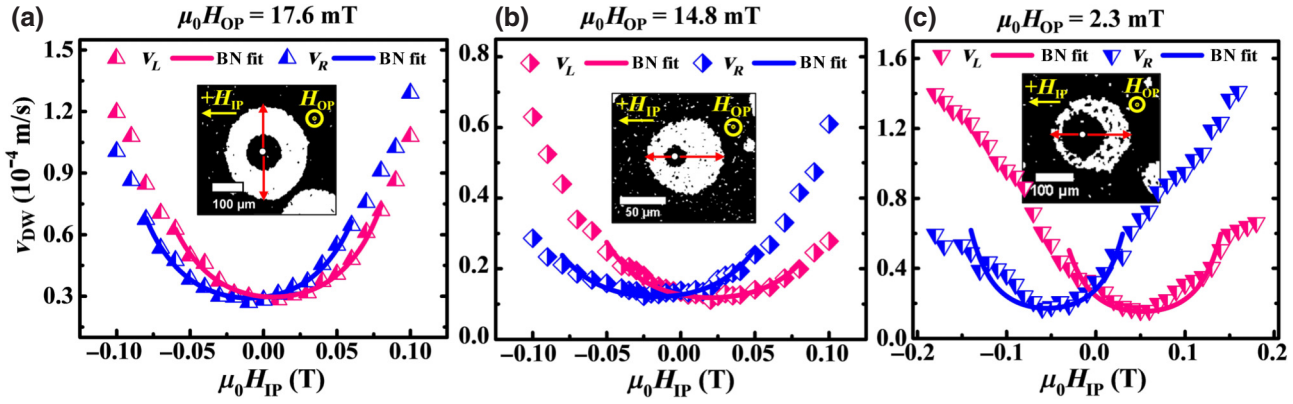

FIG. 3. The symbols pointing left (pink) and right (blue) represent the velocities of the domain walls (v_{DW}) along the left and right sides of the domains and are plotted against the in-plane bias field $\mu_0 H_{IP}$ under a constant driving field $\mu_0 H_{OP}$ for samples S1 (a), S2 (b), and S3 (c). The solid lines represent Bloch-Néel (BN) fits of the curves by the modified creep law. The inset in each figure shows the direction of domain elongation with respect to the direction of the IP field ($\mu_0 H_{IP}$). The scale bar for the domains is shown in each part separately.

the weak intra-atomic SOC of C, and (ii) a curvature-driven SOC (Δ_{curv}), whose strength can be large due to hybridization between the adjacent π and σ bonds of C atoms induced by the buckyball structure [22–24]. The fullerene molecule is composed of exactly 12 pentagons and 20 hexagons, which helps to form a closed cage structure with the proper curvature, as per Euler's theorem [25]. The π electrons of the C atoms do not contribute to the SOC, due to their quenched angular momentum, whereas the σ electrons can contribute to enhancing the SOC strength due to the overlapping of these bonds caused by the curvature [23]. Such a curvature-enhanced SOC could be a source of a finite DMI arising from the Co/C_{60} interface. We quantify the iDMI strength emanating from the Co/C_{60} interface via the asymmetric domain expansion method as proposed by Je *et al.* [37]

A system with a sizeable DMI generates a DM field ($\mu_0 H_{DMI}$), which acts in the direction radially opposite to the DW surrounding a bubble. Thus, the DM field is either canceled or enhanced under an IP bias field, resulting in faster motion of one DW (say, v_L or $\uparrow\downarrow$) and slower motion of the other (say, v_R or $\downarrow\uparrow$) along the radial direction. The evolution of domains in the presence of both IP and OP fields is found to be different for samples with and without C_{60}. For sample S1, the domains become more elongated along the direction transverse to the applied IP field, whereas for samples S2 and S3, an elongation along the longitudinal axis is observed, which is shown in the insets of Fig. 3. The distinct wall types and the nature of the chirality are quantified by measuring the displacement (S) of the wall along both the radial (x) and the transverse (y) directions [53]. Here, the parameter ϵ_1 ($= S_x^+/S_x^-$) determines the chirality of the DW, where S_x^+ and S_x^- denote the displacement of the DW along the $+H_x$ ($+H_{IP}$) and $-H_x$ ($-H_{IP}$) directions, respectively [53]. $\epsilon_1 < 1$ denotes the formation of a left-handed chiral wall, whereas, for $\epsilon_1 > 1$, a right-handed DW is formed. The other parameter, ϵ_2 ($= S_y/S_x^M$), determines the type of the wall (either Bloch or Néel), where S_y denotes the elongation along the transverse y axis and S_x^M denotes the maximum elongation along the IP field axis (i.e., the x axis) [53]. For sample S1, $\epsilon_2 > 1$ confirms the formation of a Bloch wall, whereas for samples S2 and S3, $\epsilon_2 < 1$ confirms the presence of a Néel wall. Conversion of a Bloch wall into a Néel wall requires the presence of a critical DMI field ($\mu_0 H_{DMI}$) greater than the DW anisotropy field ($= 4K_D/\pi M_s$) of the sample, where K_d is the DW shape-anisotropy energy density and M_s is the saturation magnetization. To investigate the chirality of samples S2 and S3, we calculate the parameter ϵ_1. Here, ϵ_1 is found to be less than 1 for both of the samples, which signifies a left-handed chirality of the DW, where $\mu_0 H_{DMI}$ acts in a radially inward direction.

The magnitude of $\mu_0 H_{DMI}$ can be deduced from a plot of $v_{DW}(H_{IP})$ versus $\mu_0 H_{IP}$, where, at a certain value of H_{IP}, the DW energy becomes maximum and the velocity becomes minimum; this value of H_{IP} is known as the DM field. We measure the velocity of both the left ($\uparrow\downarrow$) and the right ($\downarrow\uparrow$) DW in the three samples at a constant field $\mu_0 H_{OP}$, as shown in Fig. 3. The velocity curves are fitted by a modified creep law, where the energy-barrier scaling parameter takes account of the dependence on the IP field, written as [37]

$$v_{DW}(H_{IP}) = v_0 \exp[-\alpha (H_{OP})^{-(1/4)}], \tag{4}$$

where α is the modified energy-barrier scaling parameter, written as [37]

$$\alpha = \alpha_0 \left(\frac{\sigma(H_{IP})}{\sigma(0)}\right)^{-(1/4)} = \frac{T_{dep}}{T}(\mu_0 H_{dep})^{1/4}\left(\frac{\sigma(H_{IP})}{\sigma(0)}\right)^{-(1/4)}, \tag{5}$$

and where α_0 depends on the pinning energy in the absence of an IP bias field, whereas the IP-field-dependent DW energy $\sigma(H_{IP})$ can be expressed as [37]

$$\sigma(H_{IP})_{BN} = \sigma(0) - \frac{\delta(\pi\mu_0 M_s)^2}{8K_D}(H_{IP} + H_{DMI})^2, \quad \text{for } |H_{IP} + H_{DMI}| < \frac{4K_D}{\pi\mu_0 M_s}, \tag{6}$$

$$\sigma(H_{IP})_N = \sigma(0) + 2K_D\delta - \pi\delta\mu_0 M_s|H_{IP} + H_{DMI}|, \quad \text{otherwise.} \tag{7}$$

Here, $\sigma(0) = 2\pi\sqrt{AK_{eff}}$ is the pure Bloch-wall energy, $\delta = \sqrt{A/K_{eff}}$ is the DW width, and $K_D = t\ln(2)\mu_0 M_s^2/2\pi\delta$ is the DW anisotropy energy density. The velocity curve for the reference sample S1 is found to be very symmetric in nature [Fig. 3(a)]. We extract the value of $\mu_0 H_{DMI}$ by fitting both the left and the right velocity curves with Eq. (4) and take an average to calculate the effective DMI strength using the formula $D_{eff} = \mu_0 H_{DMI} M_s \delta$. A nonzero DMI field is found for sample S1 ($\mu_0 H_{DMI} \sim$ 8 mT) due to the different interfacial-roughness, strain, and

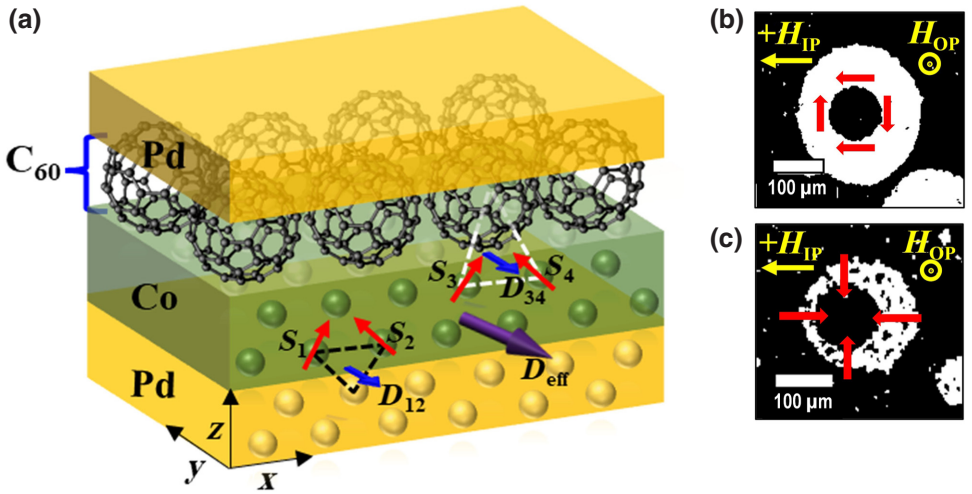

FIG. 4. (a) Schematic demonstration of effective DMI in a Pd/Co/C_{60} sample (sample S3); (b),(c) chirality of the domain walls in samples S1 (achiral Bloch wall) and S3 (chiral Néel wall), respectively. Here, the yellow and red arrows represent the directions of the applied IP field and of the spins in the DW, respectively.

growth conditions of the top and bottom Pd layers with respect to the Co layer. This corresponds to a small DMI contribution, $D_{\text{eff}} = -0.077 \pm 0.015$ mJ/m^2, for the reference sample S1. As the DMI field (approximately 8 mT) is not sufficient to overcome the critical value of the DW anisotropy field ($4K_D/\pi M_s \sim 25$ mT), sample S1 shows a Bloch wall structure as explained earlier. It is noteworthy that for symmetric samples (Pt/Co/Pt, Pd/Co/Pd), variations in the parameters of the top and bottom HM/FM interfaces (roughness, strain, etc.) may generate a significant DMI that aids in stabilizing a chiral Néel wall structure [31,54,55]. For sample S2, the insertion of a C_{60} layer shifts the velocity minimum and hence, the average of $\mu_0 H_{\text{DMI}}$ shifts to approximately 19 mT [Fig. 3(b)]. As the fullerene layer is not continuous, it increases the DMI strength slightly to -0.174 ± 0.018 mJ/m^2. Here, the critical DW anisotropy field is found to be comparable to the DMI field of the sample, which indicates the formation of an intermediate Bloch-Néel wall. However, by analyzing the parameter ϵ_2, as discussed earlier, it is found that the DW can transform to a Néel wall by acquiring a DMI field slightly higher than the critical field for sample S2. With the 1.6-nm-thick fullerene layer in sample S3, the average minima of the velocity curves shift to 53.4 mT, which leads to an enhancement of the DMI strength to -0.462 ± 0.013 mJ/m^2 [Fig. 3(c)]. Here, the critical DW anisotropy field ($4K_D/\pi M_s = 14$ mT) is found to be very small compared with the DMI field ($\mu_0 H_{\text{DMI}} = 53.4$ mT) of the sample, supporting the formation of a Néel wall with a high DW velocity in sample S3. The values of $\mu_0 H_{\text{DMI}}$, D_{eff}, and δ for all the samples are listed in Table I. The negative sign of the DMI found for a Pd/Co interface is consistent with earlier reports for $[\text{Co/Pd}]_N$ stacks [56].

To disentangle the DMI contributions originating from the bottom Pd/Co and top Co/C_{60} interfaces (if any), we prepare two control samples with the structure Pd(4 nm)/Co(0.5 nm)/Cu(t_{Cu} nm)/Pd(2 nm), where $t_{\text{Cu}} = 2$ and 5 nm. Here, Cu is used as a spacer layer due to its immiscibility with Co and its low SOC, which gives rise to a negligible or no DMI from the Co/Cu interface. Ajejas *et al.* have shown experimentally that a Co/Cu interface generates no DMI, owing to the negligible work function ($\Delta\phi \sim 6$ meV) assigned to this interface [57]. Hence the effective DMI of the control samples can be assigned to the bottom Pd/Co interface, with no additive or subtractive DMI from the top Co/Cu interface. By comparing the DMI of the Pd/Co/Cu sample with that of the Pd/Co/C_{60} sample, one can find the DMI originating from the top Co/C_{60} interface. The IP-field-dependent velocity measurements show minima in the velocity curve at 46 and 43 mT for the samples with 2 and 5-nm Cu spacer layers, respectively. This gives rise to an effective DMI (D_{eff}) $= -0.36 \pm 0.01$ mJ/m^2 for the Cu 2-nm sample and (D_{eff}) $= -0.35 \pm 0.01$ mJ/m^2 for the Cu 5-nm sample. Details of the measurement of the velocity (v_{DW}) versus the IP field ($\mu_0 H_{\text{IP}}$) for both of the control samples are presented in the Supplemental Material [36]. If we assume a negligible DMI from the Co/Cu interface, then the DMI from the bottom Pd/Co interface is $D_{\text{Pd/Co}} \sim -0.35 \pm 0.01$ mJ/m^2. Thus, comparing the DMI strength in the control samples with that in sample S3, one can conclude that a nonzero DMI ($D_{\text{Co/C}_{60}} \sim -0.11$ mJ/m^2) originates from the top Co/C_{60} interface, due to the curved-structure-induced high SOC of fullerene. To differentiate the effect of the curved structure of fullerene from that of a planar carbon (C) layer, we review the work of Li *et al.* [58]. These authors aimed to explore the effect of the insertion of a carbon

layer on the DMI and DW velocity in a Pt/Co/Ta sample and found that the DMI values for both Pt/Co/Ta and Pt/Co/C/Ta samples were similar. This reveals that only the bottom Pt/Co interface contributes to the DMI, with no contribution from the top Co/C interface. As the planar C layer lacks an improved SOC, the Co/C interface does not contribute to the DM interaction. In contrast to this, we extract a finite DMI from the Co/C_{60} interface due to its enhanced SOC induced by the curved structure of the molecule. A schematic illustration of the DMI in sample S3 is shown in Fig. 4(a), along with the chirality of the DWs for both of the samples S1 and S3 [Fig. 4(b)]. For the bottom Pd/Co interface, the DMI (D_{12}) originates from the interactions of the canted spins S_1 and S_2 of the Co layer with the Pd atoms. Hence, the DMI vector D_{12} acts along the $-y$ direction. Similarly, for the Co/C_{60} interface, D_{34} also acts along the same direction, giving rise to an additive effective DMI (D_{eff}) along the $-y$ axis. The sign of the DMI for the Co/C_{60} interface is found to be analogous to that for a Co/graphene interface, as reported earlier [8]. To understand the potential of the fullerene molecule to host a chiral wall structure, we compare the DMIs attributed to different interfaces between FMs and C-based allotropes, listed in Table S3 in the Supplemental Material [36]. If the iDMI at the Co/C_{60} interface is properly tailored, C_{60} will become a viable option for hosting chiral spin textures along with long spin-transport channels, with less effort from a device-fabrication viewpoint.

IV. CONCLUSIONS

A systematic investigation is conducted in the work presented here to comprehend the impact of the Co/fullerene interface on the magnetization-reversal mechanism, DW dynamics, and DM interaction in a $Pd/Co/C_{60}$ system. The observation of a continuous decrease in coercivity with increasing C_{60} thickness is corroborated by a reduction in the effective PMA of the samples. Relaxation measurements performed at subcoercive-field values indicate a significantly faster magnetization-reversal mechanism for samples with a high C_{60} coverage. A reduced depinning field and a DW velocity enhanced by 2 orders of magnitude seem to play a key role in the observed faster relaxation mechanism in the samples with a higher thickness of C_{60}. The chirality of the DWs is evaluated by examining the elongation axis of each domain under an IP applied field. The DW structure changes from an achiral Bloch wall (in Pd/Co/Pd) to a chiral Néel wall (in $Pd/Co/C_{60}$) on account of an enhanced DMI in samples with C_{60}. The signature of a nonzero DMI ($D_{Co/C_{60}} \sim -110\ \mu J/m^2$) emanating from the Co/C_{60} interface is the result of a curvature-enhanced SOC in the fullerene molecule. Thus the emergence of a DM interaction from the Co/fullerene interface is quite appealing from the viewpoint of both fundamental studies and the application of chiral structures in spintronic devices. We anticipate that our findings will spur the development of theoretical modeling to clarify the exact role of spherical fullerene molecules in generating a DM interaction.

ACKNOWLEDGMENTS

The authors thank Dr. Antarjami Sahoo and Mr. Shaktiranjan Mohanty for their valuable suggestions and for discussions about the research work. We also thank the Department of Atomic Energy (DAE), the Department of Science and Technology, Science and Engineering Research Board (Grant No. SB/S2/CMP-107/2013), and the Department of Science and Technology, Science and Engineering Research Board (Grant No. CRG/2021/001245), Government of India, for providing financial support.

[1] A. Fert, V. Cros, and J. Sampaio, Skyrmions on the track, Nat. Nanotechnol. **8**, 152 (2013).
[2] S. Parkin and S.-H. Yang, Memory on the racetrack, Nat. Nanotechnol. **10**, 195 (2015).
[3] X. Zhang, S. Mizukami, T. Kubota, Q. Ma, M. Oogane, H. Naganuma, Y. Ando, and T. Miyazaki, Observation of a large spin-dependent transport length in organic spin valves at room temperature, Nat. Commun. **4**, 1 (2013).
[4] L. Guo, Y. Qin, X. Gu, X. Zhu, Q. Zhou, and X. Sun, Spin transport in organic molecules, Front. Chem. **7**, 428 (2019).
[5] W. Han, R. K. Kawakami, M. Gmitra, and J. Fabian, Graphene spintronics, Nat. Nanotechnol. **9**, 794 (2014).
[6] Y. Wu, S. Zhang, J. Zhang, W. Wang, Y. L. Zhu, J. Hu, G. Yin, K. Wong, C. Fang, C. Wan, *et al.*, Néel-type skyrmion in WTe_2/Fe_3GeTe_2 van der Waals heterostructure, Nat. Commun. **11**, 1 (2020).
[7] H. Yang, G. Chen, A. A. Cotta, A. T. N'Diaye, S. A. Nikolaev, E. A. Soares, W. A. Macedo, K. Liu, A. K. Schmid, A. Fert, *et al.*, Significant Dzyaloshinskii–Moriya interaction at graphene–ferromagnet interfaces due to the Rashba effect, Nat. Mater. **17**, 605 (2018).
[8] F. Ajejas, A. Gudín, R. Guerrero, A. Anadon Barcelona, J. M. Diez, L. de Melo Costa, P. Olleros, M. A. Niño, S. Pizzini, J. Vogel, *et al.*, Unraveling Dzyaloshinskii–Moriya interaction and chiral nature of graphene/cobalt interface, Nano Lett. **18**, 5364 (2018).
[9] A. Hallal, J. Liang, F. Ibrahim, H. Yang, A. Fert, and M. Chshiev, Rashba-type Dzyaloshinskii–Moriya interaction, perpendicular magnetic anisotropy, and skyrmion states at 2D materials/Co interfaces, Nano Lett. **21**, 7138 (2021).
[10] P. Chen and G. Zhang, Carbon-based spintronics, Sci. China Phys. Mech. Astron. **56**, 207 (2013).
[11] I. Bergenti and V. Dediu, Spinterface: A new platform for spintronics, Nano Mater. Sci. **1**, 149 (2019).

[12] S. Delprat, M. Galbiati, S. Tatay, B. Quinard, C. Barraud, F. Petroff, P. Seneor, and R. Mattana, Molecular spintronics: The role of spin-dependent hybridization, J. Phys. D: Appl. Phys. **51**, 473001 (2018).
[13] S. Sanvito, The rise of spinterface science, Nat. Phys. **6**, 562 (2010).
[14] M. Galbiati, S. Tatay, C. Barraud, A. V. Dediu, F. Petroff, R. Mattana, and P. Seneor, Spinterface: Crafting spintronics at the molecular scale, MRS Bull. **39**, 602 (2014).
[15] M. Sun and W. Mi, Progress in organic molecular/ferromagnet spinterfaces: Towards molecular spintronics, J. Mater. Chem. C **6**, 6619 (2018).
[16] S. Mallik, S. Mattauch, M. K. Dalai, T. Brückel, and S. Bedanta, Effect of magnetic fullerene on magnetization reversal created at the Fe/C_{60} interface, Sci. Rep. **8**, 1 (2018).
[17] S. Mallik, P. Sharangi, B. Sahoo, S. Mattauch, T. Brückel, and S. Bedanta, Enhanced anisotropy and study of magnetization reversal in Co/C_{60} bilayer thin film, Appl. Phys. Lett. **115**, 242405 (2019).
[18] K. Bairagi, A. Bellec, V. Repain, C. Chacon, Y. Girard, Y. Garreau, J. Lagoute, S. Rousset, R. Breitwieser, Y.-C. Hu, *et al.*, Tuning the Magnetic Anisotropy at a Molecule-Metal Interface, Phys. Rev. Lett. **114**, 247203 (2015).
[19] K. Bairagi, A. Bellec, V. Repain, C. Fourmental, C. Chacon, Y. Girard, J. Lagoute, S. Rousset, L. Le Laurent, A. Smogunov, *et al.*, Experimental and theoretical investigations of magnetic anisotropy and magnetic hardening at molecule/ferromagnet interfaces, Phys. Rev. B **98**, 085432 (2018).
[20] H. Yang, A. D. Vu, A. Hallal, N. Rougemaille, J. Coraux, G. Chen, A. K. Schmid, and M. Chshiev, Anatomy and giant enhancement of the perpendicular magnetic anisotropy of cobalt–graphene heterostructures, Nano Lett. **16**, 145 (2016).
[21] M. Blanco-Rey, P. Perna, A. Gudin, J. M. Diez, A. Anadón, P. Olleros-Rodríguez, L. de Melo Costa, M. Valvidares, P. Gargiani, A. Guedeja-Marron, *et al.*, Large perpendicular magnetic anisotropy in nanometer-thick epitaxial graphene/Co/heavy metal heterostructures for spin–orbitronics devices, ACS Appl. Nano Mater. **4**, 4398 (2021).
[22] D. Huertas-Hernando, F. Guinea, and A. Brataas, Spin-orbit coupling in curved graphene, fullerenes, nanotubes, and nanotube caps, Phys. Rev. B **74**, 155426 (2006).
[23] T. D. Nguyen, F. Wang, X.-G. Li, E. Ehrenfreund, and Z. V. Vardeny, Spin diffusion in fullerene-based devices: Morphology effect, Phys. Rev. B **87**, 075205 (2013).
[24] S. Liang, R. Geng, B. Yang, W. Zhao, R. Chandra Subedi, X. Li, X. Han, and T. D. Nguyen, Curvature-enhanced spin-orbit coupling and spinterface effect in fullerene-based spin valves, Sci. Rep. **6**, 1 (2016).
[25] S. Samal and S. Sahoo, An overview of fullerene chemistry, Bull. Mater. Sci. **20**, 141 (1997).
[26] H. Liu, J. Wang, A. Chanana, and Z. Vardeny, Studies of spin transport in fullerene films, J. Appl. Phys. **125**, 142908 (2019).
[27] A. Kundu and S. Zhang, Dzyaloshinskii-Moriya interaction mediated by spin-polarized band with Rashba spin-orbit coupling, Phys. Rev. B **92**, 094434 (2015).
[28] C. Moreau-Luchaire, C. Moutafis, N. Reyren, J. Sampaio, C. Vaz, N. Van Horne, K. Bouzehouane, K. Garcia, C. Deranlot, P. Warnicke, *et al.*, Additive interfacial chiral interaction in multilayers for stabilization of small individual skyrmions at room temperature, Nat. Nanotechnol. **11**, 444 (2016).
[29] H. Yang, A. Thiaville, S. Rohart, A. Fert, and M. Chshiev, Anatomy of Dzyaloshinskii-Moriya Interaction at Co/Pt Interfaces, Phys. Rev. Lett. **115**, 267210 (2015).
[30] A. Thiaville, S. Rohart, É. Jué, V. Cros, and A. Fert, Dynamics of Dzyaloshinskii domain walls in ultrathin magnetic films, EPL (Europhys. Lett.) **100**, 57002 (2012).
[31] A. Hrabec, N. Porter, A. Wells, M. Benitez, G. Burnell, S. McVitie, D. McGrouther, T. Moore, and C. Marrows, Measuring and tailoring the Dzyaloshinskii-Moriya interaction in perpendicularly magnetized thin films, Phys. Rev. B **90**, 020402 (2014).
[32] T. H. Pham, J. Vogel, J. Sampaio, M. Vaňatka, J.-C. Rojas-Sánchez, M. Bonfim, D. Chaves, F. Choueikani, P. Ohresser, E. Otero, *et al.*, Very large domain wall velocities in Pt/Co/GdOx and Pt/Co/Gd trilayers with Dzyaloshinskii-Moriya interaction, EPL (Europhys. Lett.) **113**, 67001 (2016).
[33] Y. Yoshimura, K.-J. Kim, T. Taniguchi, T. Tono, K. Ueda, R. Hiramatsu, T. Moriyama, K. Yamada, Y. Nakatani, and T. Ono, Soliton-like magnetic domain wall motion induced by the interfacial Dzyaloshinskii–Moriya interaction, Nat. Phys. **12**, 157 (2016).
[34] A. Fert, N. Reyren, and V. Cros, Magnetic skyrmions: Advances in physics and potential applications, Nat. Rev. Mater. **2**, 1 (2017).
[35] M. Jamali, K. Narayanapillai, X. Qiu, L. M. Loong, A. Manchon, and H. Yang, Spin-Orbit Torques in Co/Pd Multilayer Nanowires, Phys. Rev. Lett. **111**, 246602 (2013).
[36] See Supplemental Material at http://link.aps.org/supplemental/10.1103/PhysRevApplied.19.044013 for a detailed discussion of the experimental methods and the structural and magnetic characterization of all the samples (S1–S3 and control samples).
[37] S.-G. Je, D.-H. Kim, S.-C. Yoo, B.-C. Min, K.-J. Lee, and S.-B. Choe, Asymmetric magnetic domain-wall motion by the Dzyaloshinskii-Moriya interaction, Phys. Rev. B **88**, 214401 (2013).
[38] A. Davydenko, A. Kozlov, A. Ognev, M. Stebliy, A. Samardak, K. Ermakov, A. Kolesnikov, and L. Chebotkevich, Origin of perpendicular magnetic anisotropy in epitaxial Pd/Co/Pd (111) trilayers, Phys. Rev. B **95**, 064430 (2017).
[39] J. Okabayashi, Y. Miura, and H. Munekata, Anatomy of interfacial spin-orbit coupling in Co/Pd multilayers using X-ray magnetic circular dichroism and first-principles calculations, Sci. Rep. **8**, 1 (2018).
[40] P. Bruno and J.-P. Renard, Magnetic surface anisotropy of transition metal ultrathin films, Appl. Phys. A **49**, 499 (1989).
[41] M. Callsen, V. Caciuc, N. Kiselev, N. Atodiresei, and S. Blügel, Magnetic Hardening Induced by Nonmagnetic Organic Molecules, Phys. Rev. Lett. **111**, 106805 (2013).
[42] Y.-L. Chan, Y.-J. Hung, C.-H. Wang, Y.-C. Lin, C.-Y. Chiu, Y.-L. Lai, H.-T. Chang, C.-H. Lee, Y. Hsu, and D. Wei,

Magnetic Response of an Ultrathin Cobalt Film in Contact with an Organic Pentacene Layer, Phys. Rev. Lett. **104**, 177204 (2010).

[43] Y.-J. Hsu, Y.-L. Lai, C.-H. Chen, Y.-C. Lin, H.-Y. Chien, J.-H. Wang, T.-N. Lam, Y.-L. Chan, D. Wei, H.-J. Lin, *et al.*, Enhanced magnetic anisotropy via quasi-molecular magnet at organic-ferromagnetic contact, J. Phys. Chem. Lett. **4**, 310 (2013).

[44] M. Johnson, P. Bloemen, F. Den Broeder, and J. De Vries, Magnetic anisotropy in metallic multilayers, Rep. Prog. Phys. **59**, 1409 (1996).

[45] T. Moorsom, M. Wheeler, T. M. Khan, F. Al Ma'Mari, C. Kinane, S. Langridge, A. Bedoya-Pinto, L. Hueso, G. Teobaldi, V. K. Lazarov, *et al.*, Spin-polarized electron transfer in ferromagnet/C_{60} interfaces, Phys. Rev. B **90**, 125311 (2014).

[46] S. K. Tiwari, V. Kumar, A. Huczko, R. Oraon, A. D. Adhikari, and G. Nayak, Magical allotropes of carbon: Prospects and applications, Crit. Rev. Solid State Mater. Sci. **41**, 257 (2016).

[47] H. Xi, K.-Z. Gao, J. Ouyang, Y. Shi, and Y. Yang, Slow magnetization relaxation and reversal in magnetic thin films, J. Phys.: Condens. Matter **20**, 295220 (2008).

[48] S. Mallick, S. S. Mishra, and S. Bedanta, Relaxation dynamics in magnetic antidot lattice arrays of Co/Pt with perpendicular anisotropy, Sci. Rep. **8**, 1 (2018).

[49] N. Chowdhury, S. Mallick, S. Mallik, and S. Bedanta, Study of magnetization relaxation in co thin films prepared by substrate rotation, Thin Solid Films **616**, 328 (2016).

[50] E. Pandey, B. B. Singh, P. Sharangi, and S. Bedanta, Strain engineered domain structure and their relaxation in perpendicularly magnetized Co/Pt deposited on flexible polyimide, Nano Express **1**, 010037 (2020).

[51] P. Chauve, T. Giamarchi, and P. Le Doussal, Creep and depinning in disordered media, Phys. Rev. B **62**, 6241 (2000).

[52] S. Lemerle, J. Ferré, C. Chappert, V. Mathet, T. Giamarchi, and P. Le Doussal, Domain Wall Creep in an Ising Ultrathin Magnetic Film, Phys. Rev. Lett. **80**, 849 (1998).

[53] D.-Y. Kim, D.-H. Kim, J. Moon, and S.-B. Choe, Determination of magnetic domain-wall types using Dzyaloshinskii–Moriya-interaction-induced domain patterns, Appl. Phys. Lett. **106**, 262403 (2015).

[54] A. W. Wells, P. M. Shepley, C. H. Marrows, and T. A. Moore, Effect of interfacial intermixing on the Dzyaloshinskii-Moriya interaction in Pt/Co/Pt, Phys. Rev. B **95**, 054428 (2017).

[55] S. D. Pollard, J. A. Garlow, J. Yu, Z. Wang, Y. Zhu, and H. Yang, Observation of stable Néel skyrmions in cobalt/palladium multilayers with Lorentz transmission electron microscopy, Nat. Commun. **8**, 1 (2017).

[56] A. Davydenko, A. Kozlov, A. Kolesnikov, M. Stebliy, G. Suslin, Y. E. Vekovshinin, A. Sadovnikov, and S. Nikitov, Dzyaloshinskii-Moriya interaction in symmetric epitaxial $[Co/Pd(111)]_N$ superlattices with different numbers of Co/Pd bilayers, Phys. Rev. B **99**, 014433 (2019).

[57] F. Ajejas, Y. Sassi, W. Legrand, S. Collin, J. P. Garcia, A. Thiaville, S. Pizzini, N. Reyren, V. Cros, and A. Fert, Interfacial potential gradient modulates Dzyaloshinskii-Moriya interaction in Pt/Co/metal multilayers, Phys. Rev. Mater. **6**, L071401 (2022).

[58] D. Li, B. Cui, J. Yun, M. Chen, X. Guo, K. Wu, X. Zhang, Y. Wang, J. Mao, Y. Zuo, *et al.*, Current-induced domain wall motion and tilting in perpendicularly magnetized racetracks, Nanoscale Res. Lett. **13**, 1 (2018).